Chapter 2

Experimental Apparatus

The search for CP violation requires a large data sample of B meson decays because many interesting decay modes have small branching fractions. B mesons are produced at a B factory (KEKB), where a high current electron (e^-) beam collides with a positron (e^+) beam. The e^+e^- collider operating at the $\Upsilon(4S)$ resonance of $\sqrt{s} = 10.58\,\mathrm{GeV}$ produces more than 10^7 $B\bar{B}$ pairs per year. The $\Upsilon(4S)$ decays to $B\bar{B}$ with a branching fraction larger than 96%. The probabilities of $\Upsilon(4S)$ decays to charged pair B^+B^- and to neutral pair $B^0\bar{B}^0$ are almost the same [19].

As the B meson mass is nearly half the $\Upsilon(4S)$ mass, B mesons are produced almost at rest in the center of mass system (cms). At KEKB, we use the asymmetric e^+ and e^- beams, so that the produced B mesons fly a certain distance before they decay. This enables us to measure the asymmetry in the proper time distribution [20] by measuring the distance between the decay vertices of the two B mesons. In addition, a lifetime measurement will be useful for eliminating continuum events and reducing combinatorial backgrounds.

On the other hand, a detector system capable of handling high event rates and large data samples is required. The detector must have state of the art capabilities in charged particle tracking, vertexing, electromagnetic calorimetry and particle identification, as well as rapid data acquisition. The Belle detector was designed to meet these requirements.

So far, the Belle detector has accumulated over 100 fb^{-1} data. Many physics results are being extracted. In the following sections, we describe the KEKB factory and the Belle detector. The Belle detector is described in more detail elsewhere [21].

2.1 The KEKB Accelerator

KEKB is an energy-asymmetric collider, which has been operated since December, 1998 at KEK, Japan. KEKB has two rings, one is 8 GeV for e^- beam, and the other is 3.5 GeV for e^+ beam, housed in the former TRISTAN tunnel. The $\Upsilon(4S)$ is produced with a

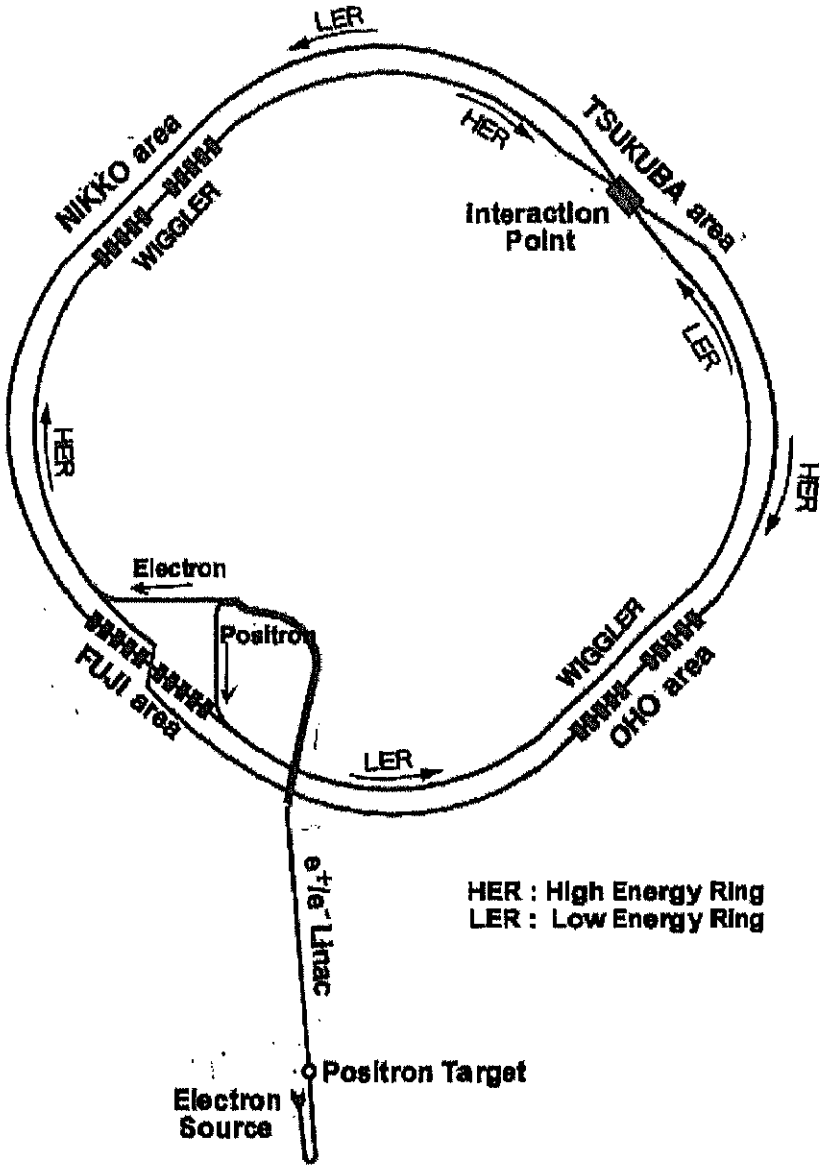

Figure 2.1: The KEKB accelerator.

Lorentz boost of $\beta\gamma = 0.425$ along the electron beam direction (defined as the z direction).

Electrons are evaporated off a filament in an electron gun, and accelerated in a linear accelerator (linac) to 8 GeV, then injected into a 3 km circumference storage ring. The next electron beam is diverted into a target about half way up the linac where they produce electron-positron pairs. The positrons are separated from electrons, and accelerated down the rest of the linac to 3.5 GeV, then injected into another storage ring. The two storage rings overlap allowing for collisions in the center of the Belle detector. The e^+ and e^- beams are collided at a finite angle of ± 11 mr. This allows us to fill all RF buckets with the beam and still avoid parasitic collisions. Another important merit of the crossing-angle scheme is that it eliminates the need for the separation-bend magnets, significantly reducing synchrotron radiation in the detector.

Major design parameters are [22]: the luminosity of $10^{34}\mathrm{cm}^{-2}\mathrm{s}^{-1}$, LER current of 2600 mA, HER current of 1100 mA, 5000 bunches injected in each storage ring, and the bunch interval is 2 ns or 60 cm in space.

The KEKB accelerator is still in the commissioning stage. Figure 2.2 shows the performance history of KEKB since the beginning of 1999. It has achieved a peak luminosity of $8.26 \times 10^{33}\ \mathrm{cm}^{-2}\mathrm{s}^{-1}$, which renewed the world record; beam current has been increased up to 1610 mA for LER, and 1006 mA for HER.

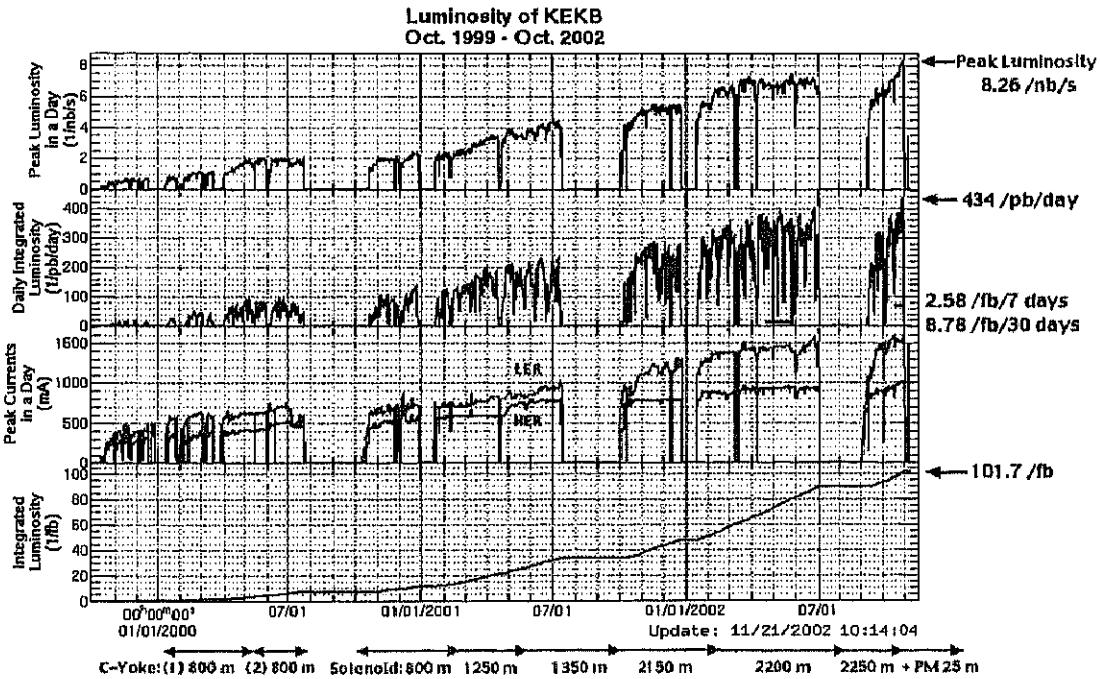

Figure 2.2: The history of the peak luminosity (the first plot) of KEKB. The histories of the integrated luminosity per day (the second plot), peak currents of the two beams (the third plot) and the accumulated luminosity (the fourth plot) are also shown.

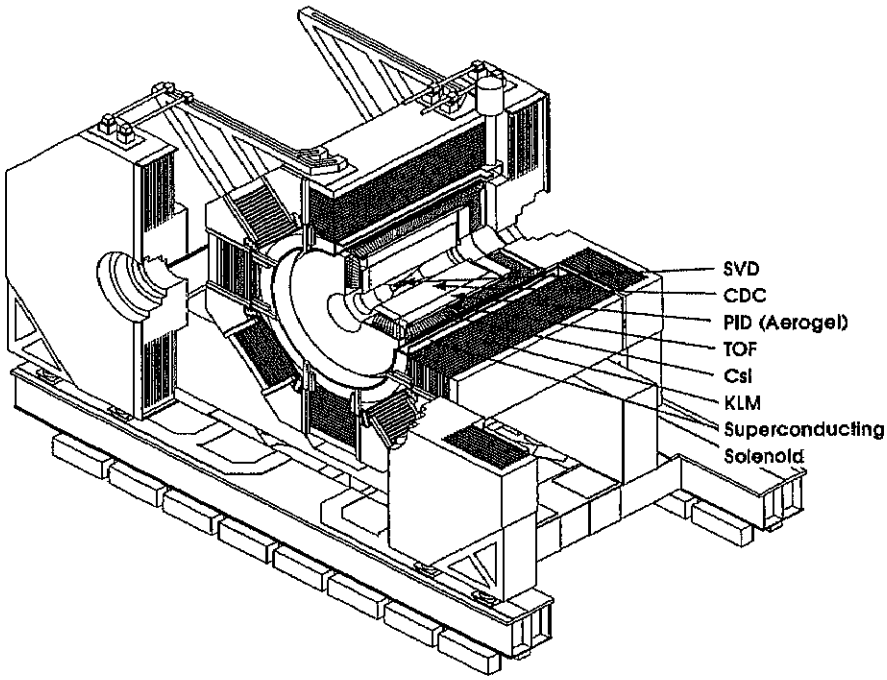

Figure 2.3: Overview of the Belle detector

2.2 The Belle Detector

Figures 2.3 and 2.4 show the configuration of the Belle detector. The detector is configured around a 1.5 T super-conducting solenoid and an iron structure surrounding the KEKB beams at the Tsukuba interaction region. The choice of the 1.5 Tesla magnetic field is a compromise between the conflicting requirements of efficient detection of low momentum particles, which curl up in the magnetic field, and a good momentum resolution for high momentum tracks. The transverse momentum distribution of charged particles from B decays peaks around 200 MeV/c, which makes the detection of low p_t tracks of great importance. The detector is almost symmetric in the azimuthal angle. It covers a polar angle region of $17° < \theta < 150°$ (θ presents the polar angle, with respect to the e^- beam, i.e. z direction).

The Belle detector was designed mainly for three purposes: position and momentum measurement of charged particles via magnetic spectroscopy; energy measurement

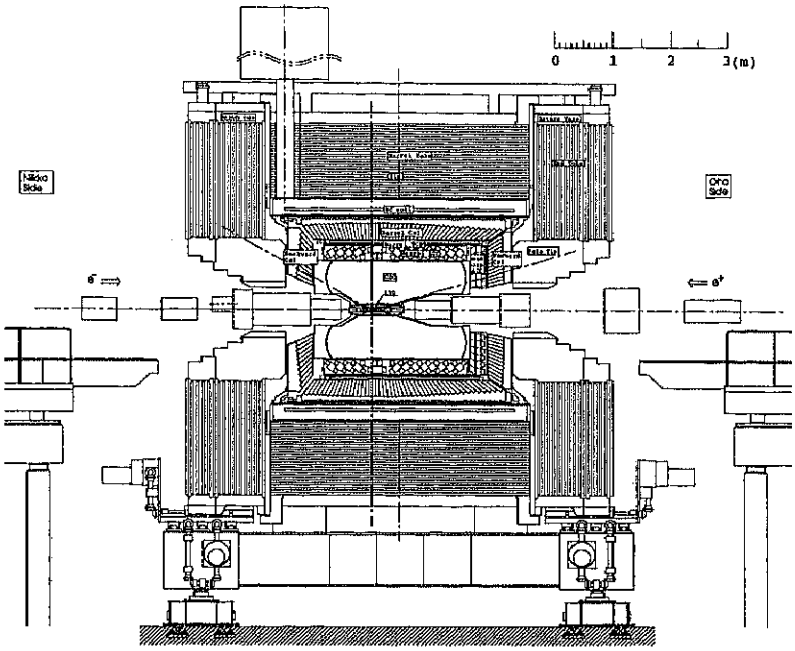

Figure 2.4: Side view of the Belle detector

of neutral particles via electromagnetic calorimetry; and identification of particle species via mass or penetration depth measurements.

To meet these requirements, the Belle detector consists of several sub-detectors: a silicon vertex detector (SVD) [23] situated just outside of a cylindrical beryllium beampipe to measure B meson decay vertices; charged particle tracking is provided by a central drift chamber (CDC) [24]; aerogel Čerenkov counters (ACC) [25] and time-of-flight counters (TOF) [26], situated radially outside of CDC, provide particle identification; an electromagnetic calorimeter (ECL) [27] comprised of CsI crystals located inside the solenoid coil provides photon detection and helps identify electrons; an iron flux-return located outside of the coil is instrumented to detect K_L^0 mesons and to identify muons (KLM) [28]; a part of the otherwise uncovered small-angle region is instrumented with a pair of BGO crystal arrays (EFC) placed in the forward and backward directions.

2.2.1 Silicon Vertex Detector (SVD)

The primary goal for the vertex detector is the measurement of the difference in the vertex positions in z direction for B meson pair with a precision of $\sim 100\,\mu$m. In addition, SVD contributes to the charged particle tracking.

Applying a reverse bias voltage to an np semiconductor junction device (i.e. a negative

voltage to the p-side) will enlarge the depletion zone. When a particle passes through the depletion region, it knocks electrons off the silicon atoms, creating electron-hole pairs. The produced electrons and holes drift to n-side and p-side falling down the potential.

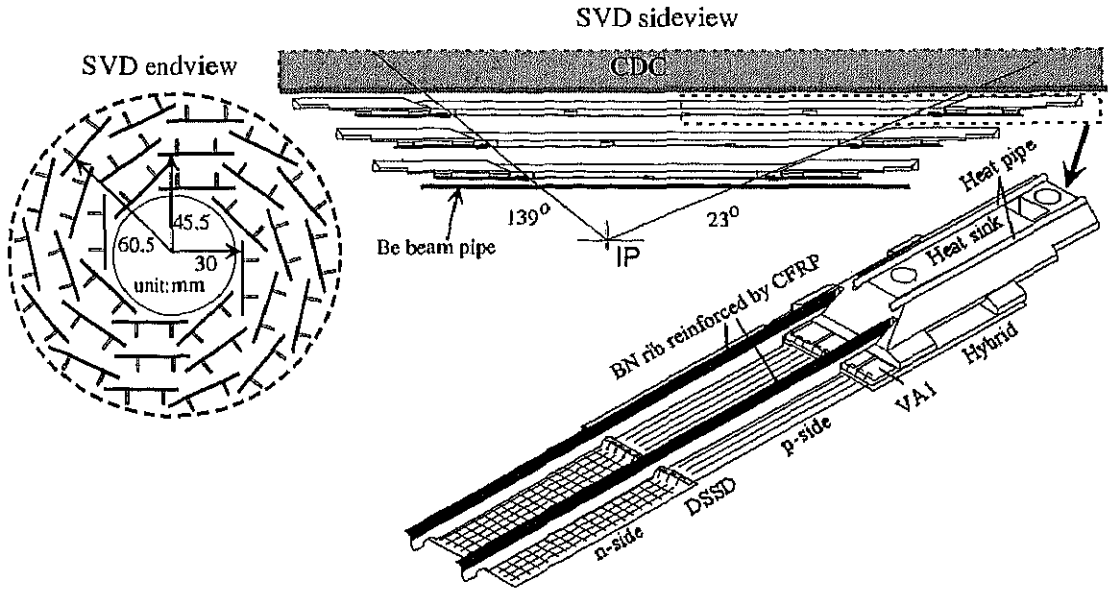

Figure 2.5: Detector configuration of SVD

Figure 2.5 shows side and end views of the SVD detector. It consists of three layers, which cover a polar angle region of $23° < \theta < 139°$, corresponding to 86 % of the full solid angle. The radii of the three layers are 30 mm, 45.5 mm and 60.5 mm. Each layer is constructed from independent ladders, (from inner to outer) consists of 8, 10 and 14 ladders respectively. Each ladder comprises double-sided silicon strip detectors (DSSDs). The standard DSSD thickness is about 300 μm. In order to achieve a vertex resolution better than 200 μm, the SVD was designed to include some overlap regions for the DSSDs in adjacent ladders.

Figure 2.6 shows a schematic diagram of the DSSD detector. One side (n-side) of the DSSDs, where n^+ strips are deposited perpendicular to the beam direction, provides the z coordinate measurement. The other side (p-side) with p^+ strips deposited orthogonal to the n-strips, e.g. aligned with the beam direction, allows us to measure the $r-\phi$ coordinate (the $r-\phi$ plane perpendicular to the e^- beam direction). A bias voltage of 75 V is applied to the n-side, while grounding the p-side. When a charged particle traverses the depletion region of the n-bulk silicon, it creates electron-hole pairs that drift to each strips, making signal hits. Aluminum readout electrodes are AC-coupled to the strips with high-resistive polysilicon. Induced charges on the electrodes by the strip charges are

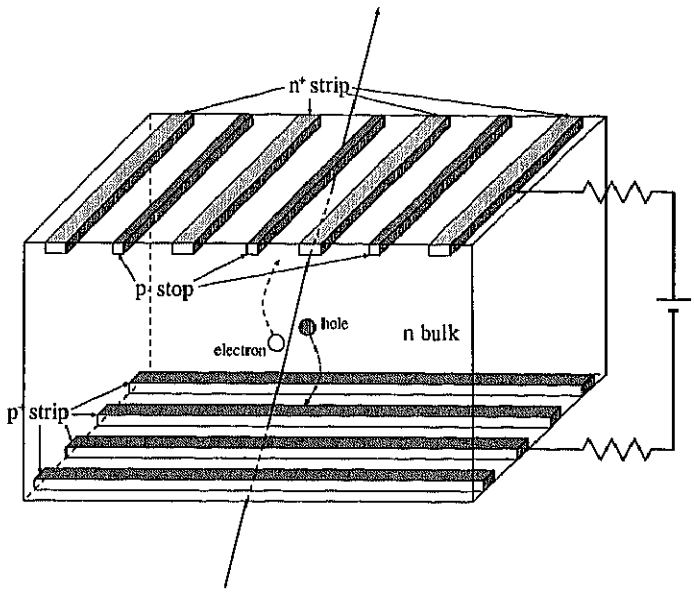

Figure 2.6: The schematic view of the double-sided silicon strip detector

readout as hit signals.

The momentum and angular dependence of the impact parameter resolution is well represented by the formulae: $(19 \oplus 50/p\beta\sin^{3/2}\theta)$ μm in the $r-\phi$ plane and $(36 \oplus 42/p\beta\sin^{5/2}\theta)$ μm in the z direction, where $\oplus$ represents a quadratic sum.

2.2.2 Central Drift Chamber (CDC)

The primary role of the CDC is the efficient reconstruction of charged particle tracks and precise determination of their momenta. The physics goals of the experiments require a momentum resolution of $\sigma_{p_t}/p_t \sim 0.5\%\sqrt{1+p_t{}^2}$ (p_t in GeV/c) for all charged particles with $p_t > 100$ MeV/c in the polar angle region of $17° \leq \theta \leq 150°$. In addition, the CDC provides information for the trigger system and particle identification in the form of dE/dx measurements for charged particles.

When a charged particle travels through a medium, energy is transfered from the particle to the atoms, causing an ionization of the medium if the amount of transfered energy is sufficient. Thus, a certain number of electron-ion pairs are created. Under an electric field, the electrons are accelerated towards the anode and the ions towards the cathode. When the electric field is strong enough to accelerate freed electrons to an energy where they are also capable of ionizing gas molecules, secondary electron-ion pairs are created. The electrons liberated in this secondary ionizations then are accelerated to produce still more ionization and so on. This results in an ionization avalanche cascade.

The number of electron-ion pairs in the avalanche is directly proportional to the number of primary electrons. Because of the great mobility of electrons and ions, a gas is the obvious medium to use for the collection of such ionizations.

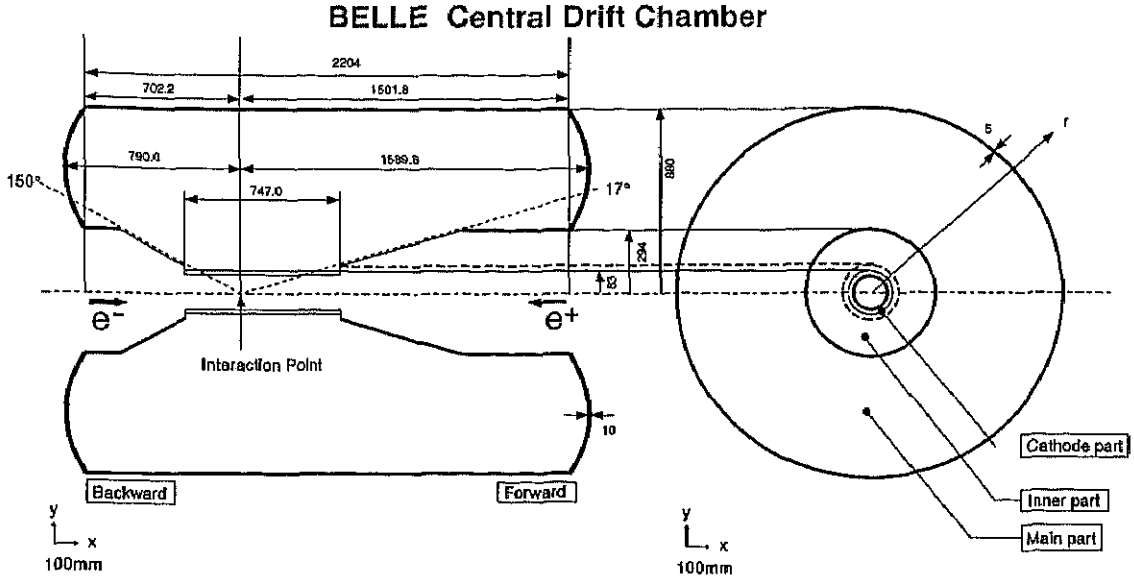

Figure 2.7: Overview of the CDC structure. The length in the figure are in units of mm.

Figure 2.7 shows the structure of the CDC detector. The CDC is asymmetric in the z direction in order to provide a polar angular coverage of $17° \leq \theta \leq 150°$. The inner and outer radii of the CDC are 8 cm and 88 cm, respectively. The CDC is a small-cell drift chamber containing a total of 50 cylindrical sense-wire layers, with 32 axial-wire layers and 18 stereo-wire layers. The axial wires are configured to be parallel to z axis, while the stereo wires are slanted by approximately ± 50 mr. This stereo angle enables us to reconstruct the particle trajectories in three-dimensions. The CDC has 8400 drift cells, which are nearly square ($16 \times 17\,\mathrm{mm}^2$), as shown in Fig. 2.9. One cell consists of one sense wire and eight electric field wires. The sense wires are gold plated tungsten of 30 μm in diameter to maximize the drift electric field, and the field wires are unplated aluminum of 126 μm in diameter to reduce the material of the chamber. The field wires produce electric fields up to the edge of the cell to simplify the drift time-to-distance relation. The electric field strength at the surface of the aluminum field wire is configured to be less than 20 kV/cm to avoid radiation damage. A mixture of He (50%) and C_2H_6 (50%) gas is filled in the CDC chamber. The use of the helium minimizes the multiple Coulomb scattering which contributes to the momentum resolution. The gas He-C_2H_6 radiation length is about 640 m and its drift velocity is 4 cm/μs. When a particle penetrates a cell, it causes an ionization avalanche, results in a large pulse of charge on the sense wire.

A charged particle traveling through the CDC will leave a series of hits in different drift cells that are used for the track reconstruction. At the innermost radii, three cathode strip layers are installed to provide the z position measurements of tracks for the trigger system.

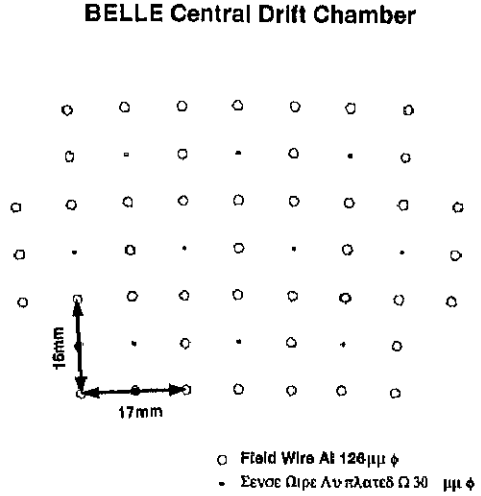

Figure 2.8: Cell structure of CDC

The spatial resolution is approximately 130 μm in the $r-\phi$ plane and less than 2 mm in the z direction. The transverse momentum resolution σ_{p_t}/p_t is $(0.20 p_t \oplus 0.29)\%$, where p_t is the transverse momentum in GeV/c. The resolution of dE/dx is 6.9% for minimum ionization particles.

The CDC hits are used for the trajectory reconstruction. In order to improve both the momentum and impact parameter resolution of charged particles, the CDC track is extrapolated towards the SVD, combined with SVD hits. The track parameters are re-calculated by using the combination of the hits on the CDC and the SVD.

At a given momentum, each particle species has a different dE/dx, as shown in Fig. 2.10. This is used for the particle identification. The separation among the different particles is most evident for $p < 1$ GeV. Thus dE/dx is primarily used for low momentum particle identification. In addition, in the higher momentum region ($p >$ 2GeV), the dE/dx is somewhat useful for the separation of particle species.

2.2.3 Aerogel Čerenkov Counter (ACC)

The threshold type Čerenkov counters, ACC system, provides particle identification, specially for $K^{\pm}$ and $\pi^{\pm}$ in the momentum region of 1.2 GeV/c $< p <$3.5 GeV/c.

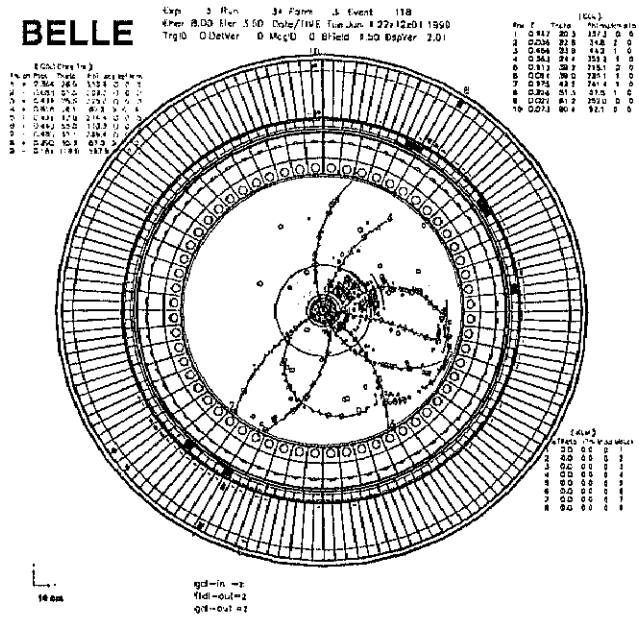

Figure 2.9: Tracks reconstructed by CDC hits and SVD hits

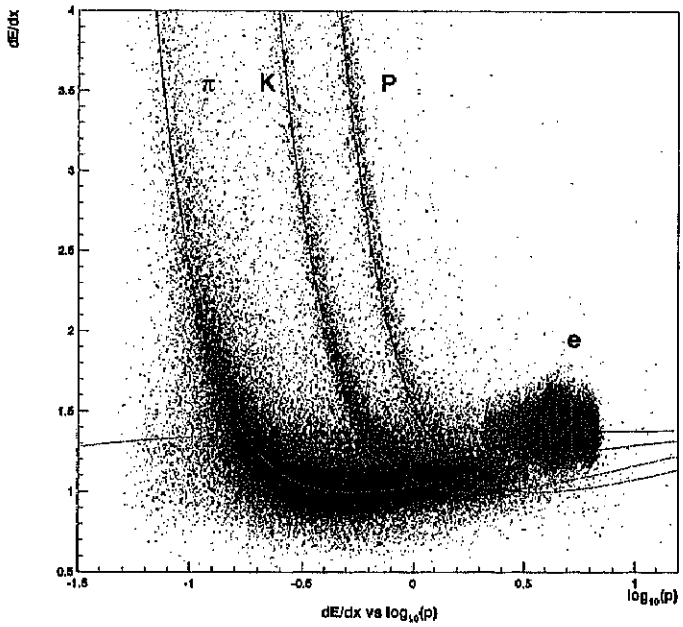

Figure 2.10: The distribution of dE/dx versus momentum from data. Each particle species has a different dE/dx.

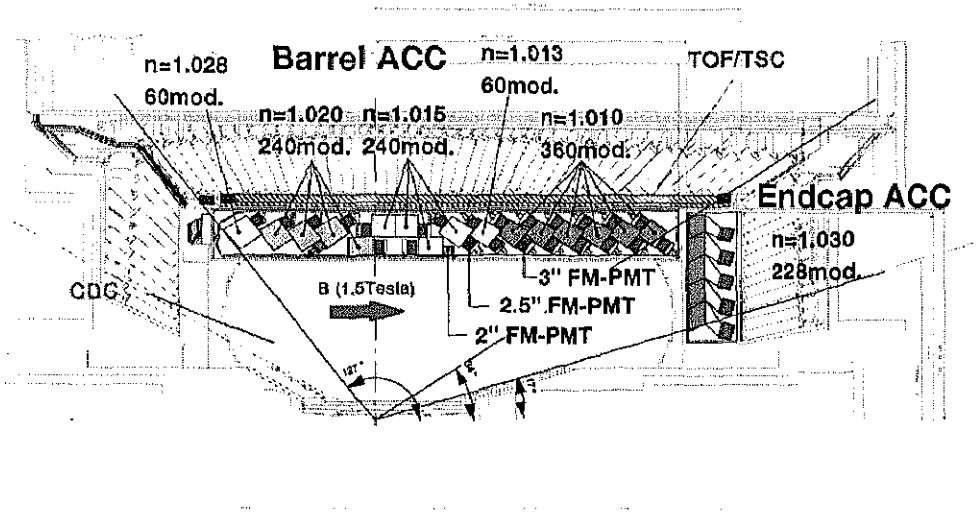

Figure 2.11: The arrangement of ACC at the central part of the Belle detector.

When a charged particle in a material medium moves faster than the speed of light in that medium, it will cause Čerenkov radiation. In the other words, a particle emitting Čerenkov radiation must have a velocity $v > c/n$, where n is the index of refraction of the medium. Since kaon (493.7 MeV) is heavier than pion (139.6 MeV), at a certain momentum the pion is above threshold while the kaon is below threshold.

In order to achieve the π/K separation in the region of 1.2 GeV/c < p < 3.5 GeV/c the ACC is required to have refractive index between those of the typical gas and the typical liquid or solid. The silica aerogel provides proper refractive indices for this requirement. The silica aerogel is a porous colloidal form of $(SiO_2)_n$ with more than 95% porosity. It is extremely light, and has a low index of reflection.

Figure 2.11 shows the configuration of the ACC system in the central part of the Belle detector. The ACC consists of 960 counter modules segmented into 60 cells in the ϕ direction for the barrel part, and 228 modules arranged in 5 concentric layers for the forward end-cap part of the detector. The refractive index of the silica aerogel are selected to be n=1.010, 1.013, 1.015, 1.020, and 1.028, depending on its polar angle region. Figure 2.12 shows the modules for the barrel and the endcap ACC. A single ACC module consists of blocks of silica aerogel contained in a 0.2 mm-thick aluminum box. The Čerenkov light generated in the silica aerogel is fed into one or two fine-mesh photomultipliers (FM-PMTs) attached to the aerogel radiator modules.

In the designed momentum region, the ACC K/π separation is correct between 85%

a) Barrel ACC Module

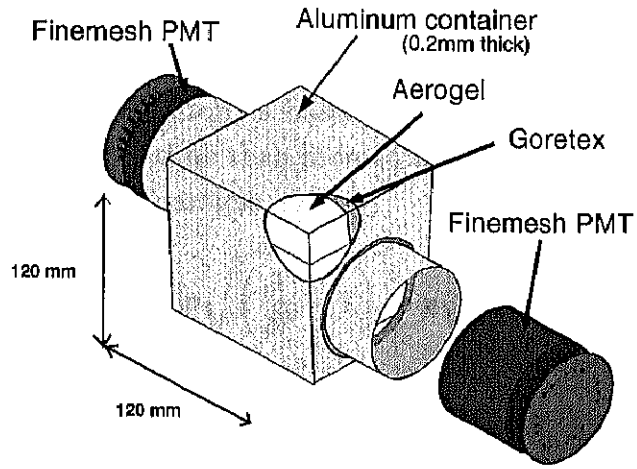

b) Endcap ACC Module

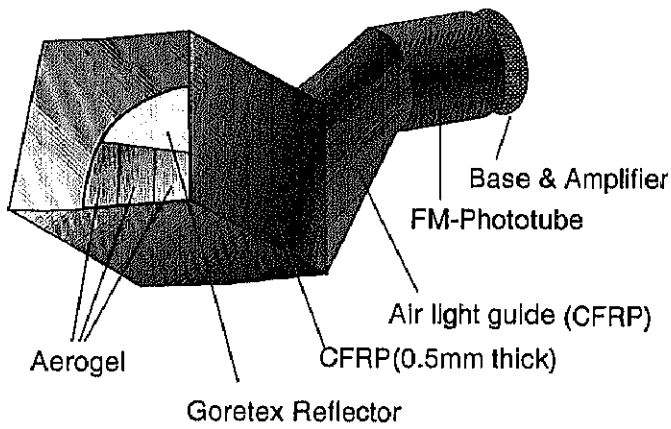

Figure 2.12: Schematic drawing of a typical ACC counter module: (a) barrel and (b) end-cap ACC.

and 95%.

2.2.4 Time of Flight Counter (TOF)

A time-of-flight (TOF) detector using plastic scintillation counters provides particle identification for particle momentum below 1.2 GeV/c, which encompasses 90% of the particles produced in $\Upsilon(4S)$ decays. In addition to particle identification, the TOF counters provide fast timing signals for the trigger system.

The TOF particle identification is based on the timing measurement. At a given momentum, kaon takes longer time than pion to travel the same distance. From the time of flight T, we can deduce the particle mass by

$$m = p\sqrt{\left(\frac{1}{\beta^2} - 1\right)} = p\sqrt{\frac{T^2}{L^2} - 1}, \tag{2.1}$$

where L is the flight length.

Scintillators are widely used in particle detection. As a particle passes through a scintillator, it excites the atoms and molecules making up the scintillator, causing light to be emitted (i.e scintillation). When the scintillator is coupled to a photomultiplier, these scintillations can be converted into electrical pulses which can then be analyzed and counted electronically to give information concerning the incident particle.

The TOF system consists of 128 TOF counters and 64 TSC counters. Two trapezoidlly shaped TOF counters and one TSC counter, with a 1.5 cm intervening radial gap, form one module as shown in Fig. 2.13 and Fig. 2.14. The 1.5 cm gap between the TOF counters and TSC counters was introduced to isolate TOF from photon conversion backgrounds by taking the coincidence between the TOF and TSC counters. Electrons and positrons created in the TSC layer are impeded from reaching the TOF counters due to this gap in a 1.5 T field. The TOF modules are individually mounted on the inner wall of the barrel ECL container. The width of the TOF counter is approximately 6 cm. In total 64 TOF/TSC modules located at a radius of 1.2 m from the interaction point cover a polar angle ranging from 34° to 120°. The TOF and TSC scintillators were wrapped with one layer of 45 μm thick polyvinyl film for light tightness and surface protection. This thin wrapping minimizes the dead space between adjacent TOF counters.

Figure 2.15 shows a block diagram for the TOF front-end electronics (TOFFEE). Each photomultiplier (PMT) signal is split into two. One is sent to a charge-to-time converter (QTC), and then to a multihit TDC for charge measurement. The other goes to generate two output signals by application of different threshold levels: a high level (HL), and a

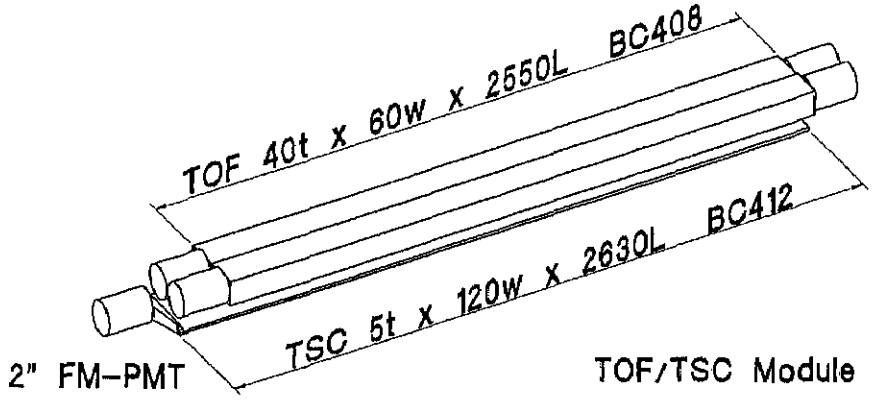

Figure 2.13: Schematic diagram of a TOF/TSC module.

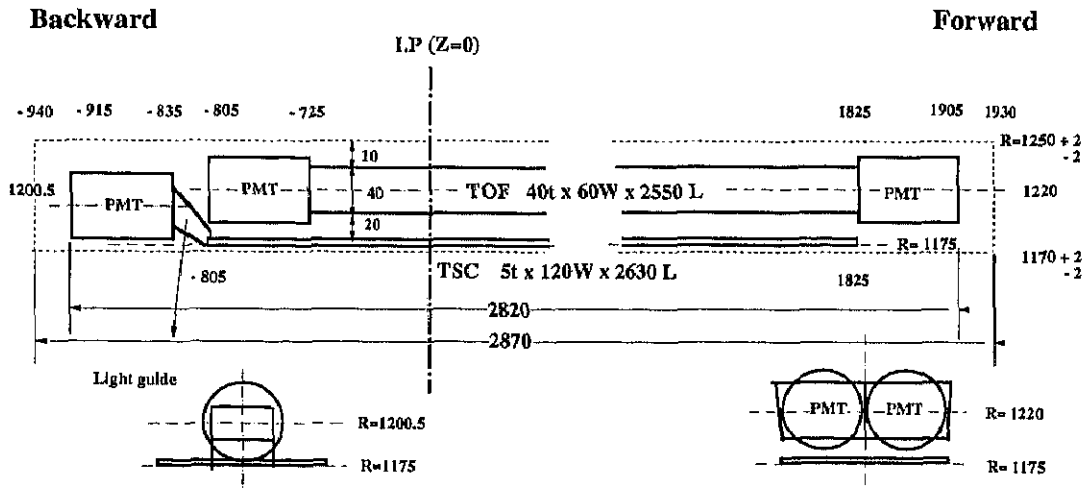

Figure 2.14: Side-view of a TOF/TSC module.

low level (LL). While the LL signal is fed to a time-stretcher for time measurement, the HL signal is used to provide a gate to the QTC. This double threshold scheme provides a robust and deadtime-less readout system for TOF signals, and also allows us to get clean event timing, even in the high rate photon background condition of KEKB.

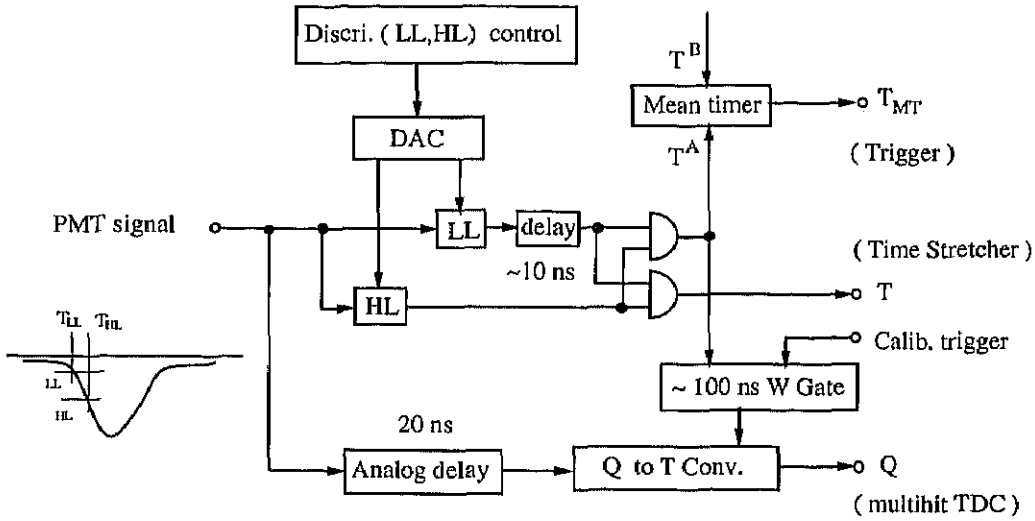

Figure 2.15: Block diagram of a single channel to TOF front-end electronics

Figure 2.16 shows a block diagram of the time stretcher (TS) TDC scheme. The TS circuit expands the time interval T between the TOF signal and one of the rising edges of TS reference clock by a factor of 20. The expanded timing edges are then readout with the Belle standard 0.5 ns LSB TDC, providing a 25 PS LSB time measurement. The TS reference clock with an approximate 16 ns period and a time jitter of 20 ps, is generated from the KEKB RF signal of 508.9 MHz. A collision bunch number from 0 to 8 is determined in off-line analysis. Due to the small expansion factor of 20 and the use of a 16 ns clock, this system provides a virtually deadtime-less TDC (1 μs). The gated LL signals from the two ends of a counter are mean-timed and coincidenced with the TSC signal to provide a fast event timing signal to the CDC. The jitter of the mean time is smaller than 3.5 ns. Furthermore, it is reduced to 0.5 ns after correction for the hit position in TOF counters.

Figure 2.17 shows time resolutions for forward and backward PMTs and for the weighted average time as a function of z. The resolution for the weighted average time is about 100 ps with a small z dependence. Figure 2.18 shows the mass distribution for each track in hadron events calculated using Equation 2.1, where p and L are momentum and path length of the particle determined from the CDC track fit assuming the muon mass, respectively. Clear peaks corresponding to $\pi^{\pm}$, $K^{\pm}$ and protons are seen. The

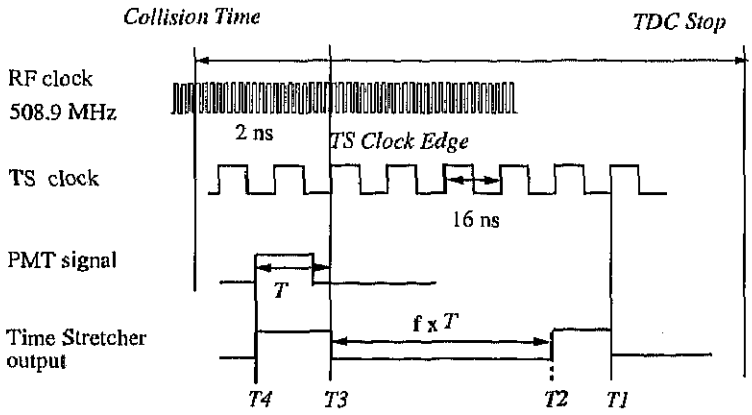

Figure 2.16: Time stretcher TDC scheme

results from data (data points) are in good agreement with a Monte Carlo prediction (histogram) obtained by assuming $\sigma_{TOF} = 100$ ps.

The minimum transverse momentum to reach the TOF counters is about 0.28 GeV/c. Conversely, as the particles become more energetic, their mass differences become less evident. For $L_{path} = 1.2$ m, and $\Delta t = 100$ ps, to satisfy the 3σ separation, the particle momentum is required to be less than

$$p_{max} < \sqrt{\frac{\Delta m_{K\pi}}{3} \frac{L_{path}}{2c} \frac{1}{\Delta t}} = 1.22\,\mathrm{GeV/c}.$$

Thus, the TOF serves as an PID device for the particles having a momentum 0.28 GeV/c $< p <$ 1.2 GeV/c.

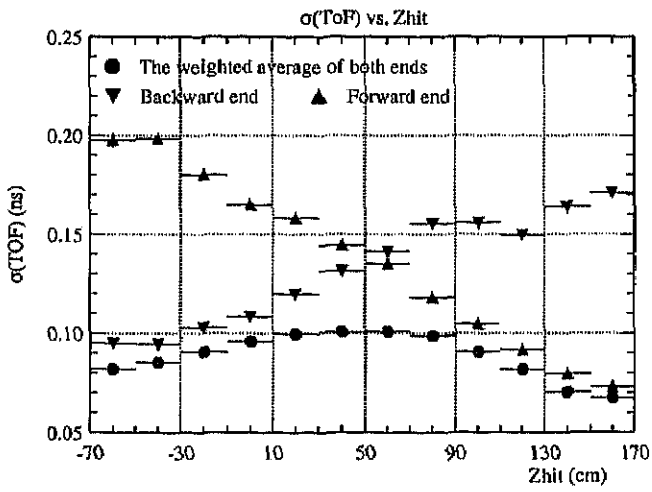

Figure 2.17: Time resolution for μ-pair events.

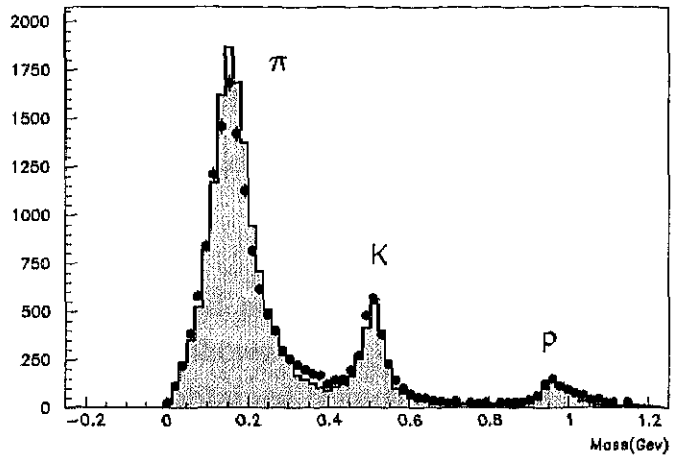

Figure 2.18: The mass distribution from TOF measurements for particle momenta below 1.2 GeV/c. The data points are obtained from hadronic events. The hatched histogram is for MC prediction by assuming the time resolution of 100 ps.

Since the RF clock is used for the whole KEKB accelerator timing control, it should, in principle, be synchronized with the beam collisions. However, the beam phase is affected by the KEKB operation condition. To measure times of flight with high precision, the beam collision time (t_0) is needed to be determined for each event precisely. t_0 is given by

$$t_0 = t_{obs} - t_{pred},$$

where t_{obs} is the observed flight time, t_{pred} is the time of flight predicted by using the track path length. Previously, t_0 was only determined during the off-line processing (Level-4), and relied on a full CDC track reconstruction that is first made available on the primary DST (Data Summary Table). This scheme requires a secondary DST production for the application of run by run t_0 correction. In order to speed up the data process, we develop a new scheme to determine t_0 in the on-line stage (at Level-3) before the primary DST production. Because it is an on-line process, it is important that the required CPU time is minimized.

At the on-line Level-3 level, only information from a fast tracking algorithm, used primarily to reduce garbage events in advance the primary DST production, is available. This dose not provide precise track information. Therefore, we had to confirm the feasibility of the t_0 determination using the fast tracking information. For this study, the $e^+e^- \to \mu^+\mu^-$ data samples are used.

First, we select clean μ-pair events with minimum CPU time. Here we include the trigger information in a fast μ-pair selection routine. The selection criteria is listed as below.

1. The number of charged tracks having a momentum $p > 9.25$ GeV/c, is two.

2. Total energy observed in ECL is required to be less than 2.0 GeV.

3. The angle between the two tracks is required to be smaller than 10°.

4. μ-pair trigger is fired

All of these can be easily obtained at the Level-3 level, so not much more additional CPU time is taken. Figure 2.19 shows the t_0 distributions, before and after the μ pair selection, compared with the t_0 obtained from the full CDC track reconstruction. Then

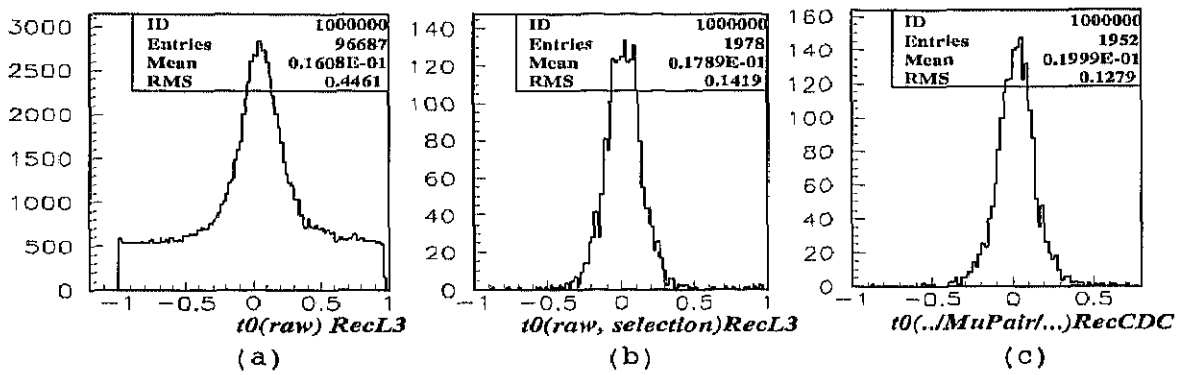

Figure 2.19: The t_0 distribution for μ-pair events by using a fast tracking algorithm (a) before the μ-pair selection (described in text) (b) after the μ-pair selection. The t_0 distribution obtained from the full CDC track reconstruction is also shown in (c).

the distribution is further fitted to a single Gaussian to determine t_0.

We confirmed that our on-line t_0 determination provides sufficient precision with little additional CPU time. It meets the requirements of the on-line process.

2.2.5 Particle Identification (PID)

In Belle, the K/π identification is carried out by combining information from three nearly-independent measurements:

- dE/dx measurements by the CDC
- times of flight measured by TOF
- measurements of the number of photoelectrons (N_{pe}) in the ACC

We make probability density functions (PDF) for the discriminant beforehand. Based on each PDF, likelihood probabilities for each measurement are calculated. The product of

the three likelihoods yields the overall likelihood probability for being a kaon or a pion, $\mathcal{L}_K$ or $\mathcal{L}_\pi$.

A particle is identified as a kaon or a pion by cutting on the likelihood ratio,

$$pid(K,\pi) = \frac{\mathcal{L}_K}{\mathcal{L}_K + \mathcal{L}_\pi}.$$

A track is more kaon-like than pion-like if $pid(K,\pi) > 0.5$. For a typical analysis, particles are identified as kaons if $pid(K,\pi) > 0.6$ and pions if $pid(K,\pi) < 0.4$.

The efficiency and fake rate are studied with $D^{*+} \to D^0\pi^+$, and $D^0 \to K^-\pi^+$ [29]. It is found that the efficiency and fake rate are slightly momentum-dependent. In general, for a pion with a momentum of 0.5-4.0 GeV/c, the efficiency is $89.22 \pm 0.07\%$ while the fake rate is around $10.00 \pm 0.07\%$.

2.2.6 Electromagnetic Calorimeter (ECL)

The main purpose of the electromagnetic calorimeter is the detection of photons with high efficiency and good resolutions both in energy and position. Electron identification in Belle relies primarily on a comparison of the charged particle momenta and the energy deposits in the electromagnetic calorimeter. A good electromagnetic energy resolution results in better hadron rejection. High momentum π^0 detection requires the separation of two nearby photons and a precise determination of their opening angle. This requires fine-grained segmentation in the calorimeter.

A high energy photon in matter converts into a pair of electron and positron which then emit energetic bremsstrahlung photons. These photons, in turn, will convert into further e^+e^- pairs, and so on. The result is a shower of photons, electrons and positrons. This continues until the energies of the pair-produced electrons and positrons drop below the critical energy, there, the e^+e^- pairs will preferentially lose their energy via atomic collision rather than bremsstrahlung emission, thus halting the cascade.

Thallium (Tl) doped CsI crystal is chosen for the ECL detector. CsI (Tl) crystals have various nice features such as a large photon yield, weak hygroscopicity, mechanical stability and the moderate price.

Figure 2.20 shows the overall configuration of the Belle calorimeter (ECL). It consists of the barrel section of 3.0 m in length with the inner radius of 1.25 m and the annular end-caps at $z = +2.0$ m and $z = -1.0$ m from the interaction point. The entire ECL system contains 8736 CsI (Tl) counters. Each crystal has a tower-like shape and is arranged so that it points almost to the interaction point. There is a small tilt angle $\sim 1.3°$ in

the θ and ϕ directions in the barrel section to avoid photons escaping through the gap of the crystals. End-cap crystals are tilted by $\sim$ 1.5° and $\sim$ 4° in the θ direction in the forward and backward sections, respectively. The calorimeter covers a polar angle region of $17° < \theta < 150°$, corresponding to a total solid-angle coverage of 91%. Small gaps between the barrel and end-cap crystals provide a pathway for cables and room for supporting members of the inner detector. The loss of solid angle associated with these gaps is approximately 3% of the total acceptance.

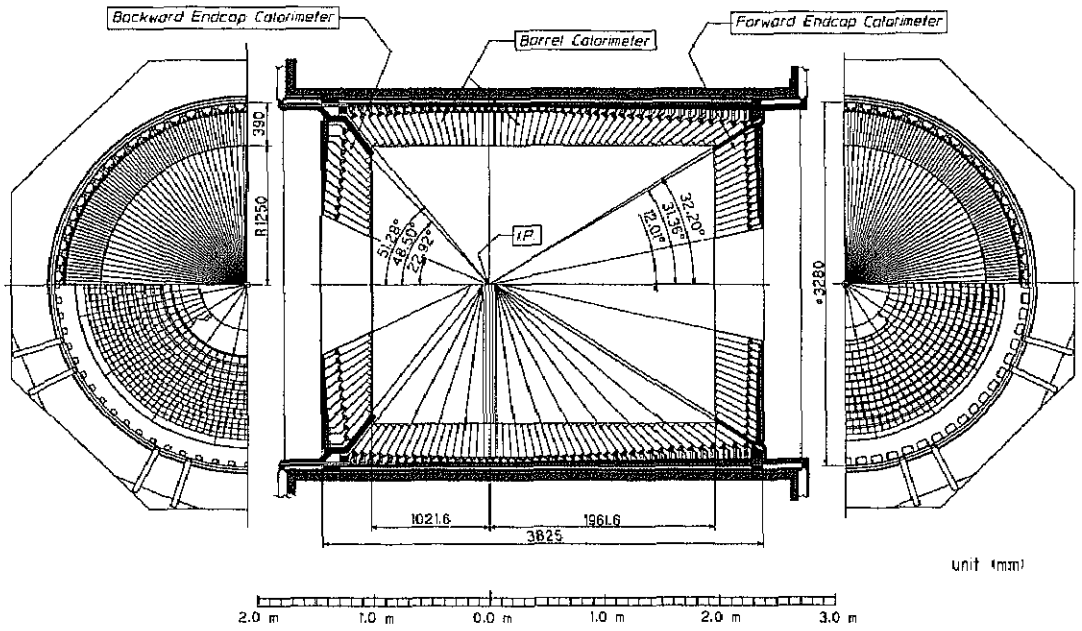

Figure 2.20: Overall configuration of ECL detector.

Electron Identification

The most significant signature of electrons is the energy deposit in the ECL by electromagnetic shower associated with a charged track in the CDC. Since most electron energy is lost by causing the electromagnetic shower in the ECL, the E/p distribution, where E is ECL cluster energy, and p is reconstructed momentum by the CDC, tends to peak at 1 for electrons, while it does not for hadrons. In addition, the lateral spread of the electromagnetic shower differs from the hadronic shower, since the radiation length of the electron is smaller than the interaction length of the hadron. It is another signature for electron identification, and can be parameterized by $E9/E25$, where $E9$ is the total energy in a 3×3 crystal matrices, and $E25$ is the total energy in a 5×5 crystal matrices. Furthermore, the dE/dx distribution is also useful for distinguishing electrons from other

charged hadrons or muons. Figure 2.21 shows the E/p, $E9/E25$ and dE/dx distributions for electrons (solid) and charged pions (dashed).

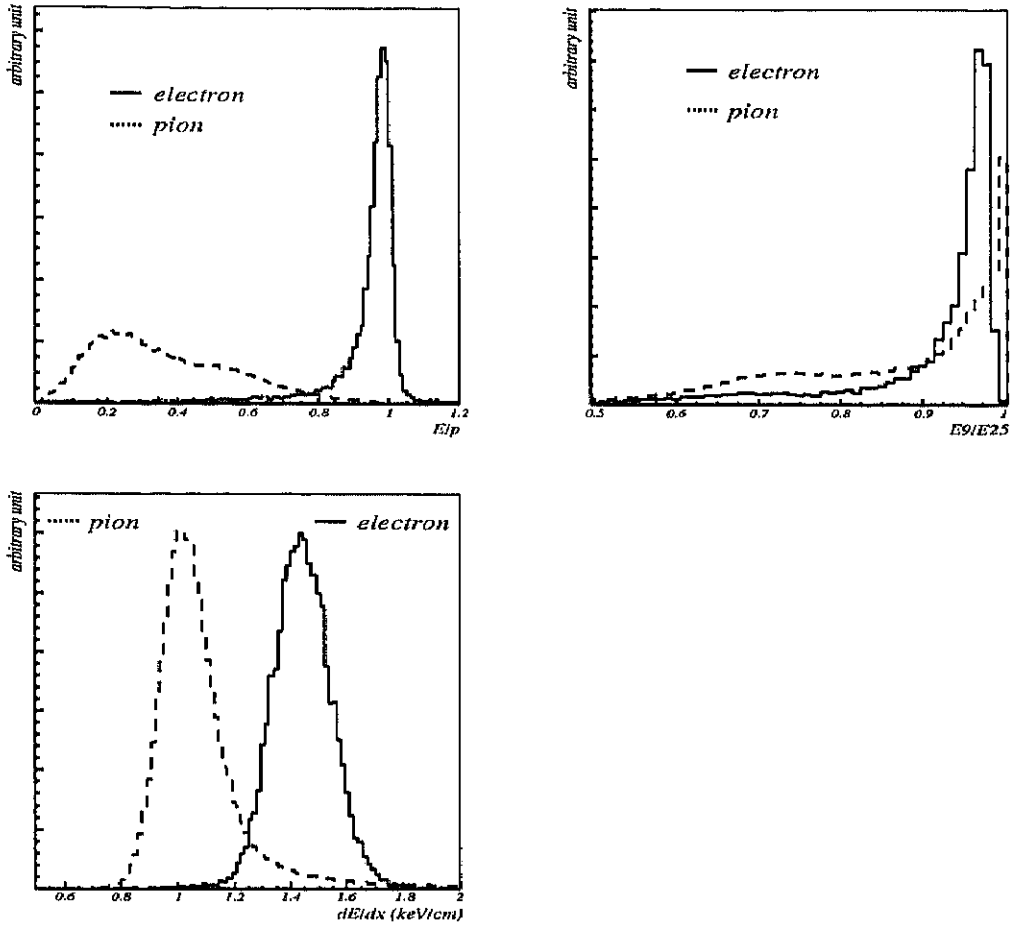

Figure 2.21: The E/p (upper left), $E9/E25$ (upper right) and dE/dx (bottom) distributions for electrons (solid) and charged pions (dashed) from data. For electrons, a sample of radiative Bhabha is used, while for charge pions, a sample of $K_s \to \pi^+\pi^-$ decays in hadronic events is used.

In Belle, electrons are identified by means of a likelihood ratio, based on

- the ratio of energy deposited in the ECL to charged track momentum measured by the CDC
- transverse shower shape at the ECL
- the matching between a cluster at the ECL and charged track position extrapolated to the ECL
- dE/dx measured by the CDC; light yield in the ACC; and the TOF measurements.

The likelihood ratio (eid) is calculated by

$$eid \equiv \frac{\mathcal{L}_e}{\mathcal{L}_e + \mathcal{L}_{non-e}},$$

where $\mathcal{L}_e$ and $\mathcal{L}_{non-e}$ are the combined likelihood for being an electron and non-electron. For a momentum greater than 1 GeV/c, the electron identification efficiency with eid >0.5 is maintained to be above 90% while a fake rate is measured to be less than 1%.

The more detailed description of electron identification is given in [30].

2.2.7 K_L and Muon Detector (KLM)

The KLM detector system was designed to identify K_L mesons and muons with high efficiency over a broad momentum range greater than 600 MeV/c. Also, the KLM is the containment of solenoid's return flux.

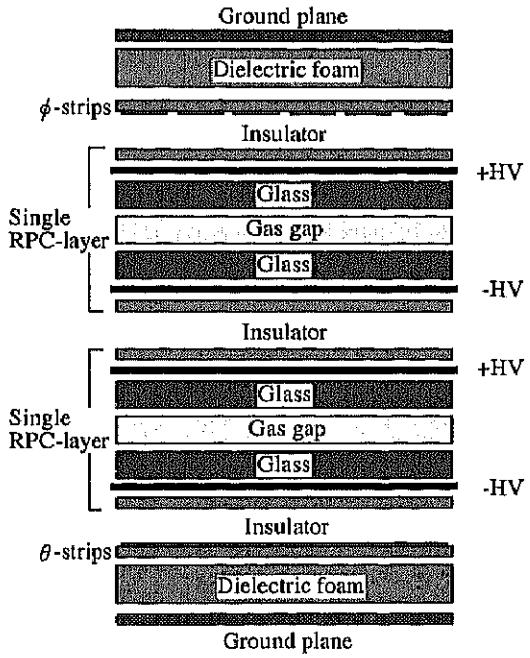

Figure 2.22: Cross section of a KLM super-layer

The KLM detector consists of alternating layers of charged particle detectors and 4.7 cm thick iron plates. There are 15 detector layers and 14 iron layers in the octagonal barrel region and, 14 detector layers in each of the forward and backward end-caps. The iron plates provide a total of 3.9 interaction lengths of material for a particle traveling

normal to the detector plane. The electromagnetic calorimeter, ECL, provides an additional 0.8 interaction length of material to convert K_L mesons. K_L interacts in the iron or ECL, producing a shower of ionizing particles. The location of this shower determines the direction of K_L. In addition, the multiple layers of charged particle detectors and iron allow the discrimination between muons and charged hadrons ($\pi^{\pm}$ or $K^{\pm}$) based on their range and transverse scattering. On average, muons travel much farther with smaller deflections than strongly interacting hadrons.

The detection of charged particle is provided by glass-electrode resistive plate counters (RPCs). Resistive plate counters have two parallel plate electrodes with high bulk resistivity separated by a gas-filled gap. In the streamer mode, an ionizing particle traversing the gap initiates a streamer in the gas that results in a local discharge of the plates. This discharge is limited by the high resistivity of the plates and the quenching characteristic of the gas. The discharge induces a signal on external pickup strips, which are used to record the location and time of the ionization. Figure 2.22 shows the cross section of a super-layer, in which two resistive plate counters are sandwiched between the orthogonal θ and ϕ pickup-strips with the ground planes for signal reference and proper impedance. The strips are roughly 5 cm wide. This unit structure of two RPCs and two readout-planes is enclosed in an aluminum box. Each RPC is electrically insulated with a double layer of 0.125 mm thick mylar. Signals from RPCs are picked up by copper strips above and below the pair of RPCs, providing a three-dimensional space point for particle tracking. Interaction length of particles as they travel through the iron is typically a few centimeters. This sets the scale for the desired spatial resolution of the KLM.

To identify K_L, a cluster must be observed in the KLM. Tracks of charged particles measured in the CDC are extrapolated into the KLM, the clusters within 15° of an extrapolated charged particle track are excluded from K_L cluster candidates. For an isolated cluster, the center of gravity of the hits is calculated and used to determine the direction of the cluster from the interaction point. Figure 2.23 shows an example of an event where a K_L is identified in the KLM.

Muon Identification

Muon identification is primarily based on the following facts. Due to the small electromagnetic cross sections (1/40000 of that of electron) and lack of hadronic interaction, muons are more penetrating than pions which are the dominant background for muon identification. The extrapolated track from the CDC is associated to the hits on the KLM. In addition, due to small interactions, muons are scarcely scattered by the KLM

material during traversing the KLM, thus the hit positions on the KLM PRCs can be assumed not to be much deviated from the geometrical expectation by the CDC track trajectory and the KLM RPC positions. We extrapolate the CDC track by assuming the particle being muon, and if the real species of the particle is pion, the deviation of the real hit positions from those of expectation becomes large. More details are described in [31].

Figure 2.23 also shows an example of an event where a muon is identified in the KLM.

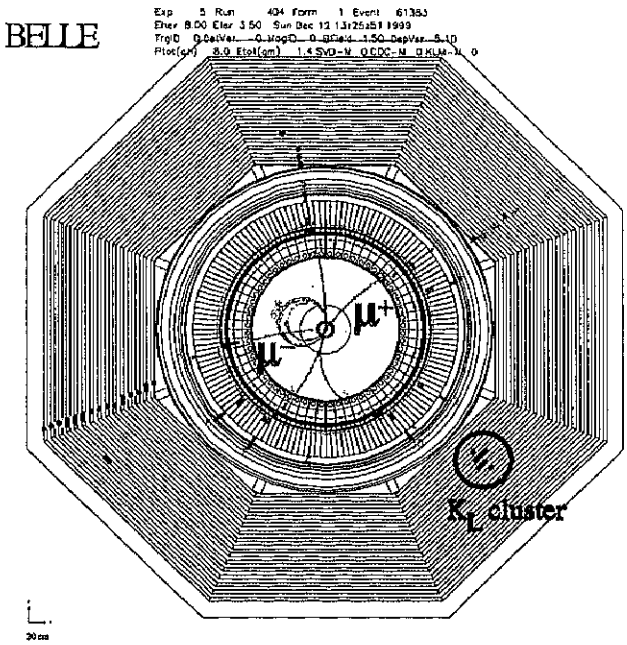

Figure 2.23: K_L candidate and muon candidates displayed in the $r - \phi$ plane. The K_L candidate has no associated tracks in the CDC. The muon candidates penetrate KLM layers and can be associated with tracks in the CDC.

2.2.8 Extreme Forward Calorimeter (EFC)

In order to improve the experimental sensitivity to some physics processes, the extreme forward calorimeter, EFC, is needed to further extend the polar angle coverage ($17° < \theta < 150°$) of ECL. The EFC covers the polar range from 6.4° to 11.5° in the forward direction, and 163.3° to 171.2° in the backward direction. The EFC detector is attached to the front faces of the cryostats of the compensation solenoid magnets of the KEKB accelerator, surrounding the beam pipe. The EFC is also required to function as a beam mask to reduce backgrounds for the CDC. In addition, the EFC is used for a fast luminosity monitor to tune the KEKB accelerator conditions.

Since the EFC is placed in the very high radiation-level area around the beam pipe near the interaction point, it is required to be radiation-hard. We adopt the bismuth germanate, $Bi_4Ge_3O_{12}$ (BGO) crystal calorimeter, which satisfies the requirement of radiation-hard and provides good energy resolutions for electrons and photons.

Both the forward and backward EFC consist of BGO crystals segmented into 5 regions in the θ direction and 32 regions in the ϕ direction, in order to provide a better position resolution. Typical cross-section of a crystal is about 2×2 cm^2 with a 12.0 radiation length for forward and a 10.5 radiation length for backward.

2.3 MC Simulation

Monte Carlo (MC) study is an important procedure for the analysis. It helps us to understand the features of signal events as well as its backgrounds. MC simulation is used for various purposes, such as determining the candidate selection, optimizing the separation between signal and backgrounds, background estimates, and so on. According to our studies, the Belle MC simulation is consistent with experiment data well.

The MC production of the Belle experiment includes three parts: QQ98 [32] generator or EvtGen [33]; Geant [34] based detector simulation (GSIM); and reconstruction for track/cluster (RECON).

The generator QQ98 is originally developed by the CLEO group, and modified by Belle [35]. Recently, another generator EvtGen is widely used. In contrast to QQ98, EvtGen partially uses decay amplitudes for the description of a subset of decay. The generators generate the initial four vectors, event vertices and the general topology of $B\bar{B}$ events. The programs contain all the known information about the physics of B meson decays such as particle masses, lifetimes, and branching fractions. They also contain the information about the initial parameters of KEKB such as the electron and positron energies.

The event history of EvtGen or QQ98 is used as an input to the GSIM simulation program which converts them to hits. The GSIM is a Geant based program that has information on the geometry and material of the Belle detectors. Inside the GSIM, each generated particle is propagated through various detector elements keeping track of the multiple scattering, interaction with detector materials, electron conversion and properly decaying long lived pions and kaons.

Finally, the hits are passed to the event reconstruction (RECON) program to create the final state four vectors.